RSC Applied Interfaces

ROYAL SOCIETY OF CHEMISTRY

PAPER

View Article Online
View Journal | View Issue

Cite this: *RSC Appl. Interfaces*, 2025, **2**, 1889

Insights from theory and experiments on the dynamics of controlled *in situ* polymerization of pyrrole at the liquid–liquid interface

Aiswarya Chandran,[a] Hashima Madathingal,[a] P. N. Bala Subramanian *[b] and Mini Mol Menamparambath *[a]

The controlled diffusion and precise assembly of nanoparticles, polymers, and conventional surfactants at liquid–liquid (L–L) interfaces have significant potential in research domains such as oil recovery, electro-optics, and liquid electronics. Apart from this, L–L interfaces have been explored as a promising strategy to tune the nanostructure of conductive polymers and their hybrids in an *in situ* manner. The present work focuses on understanding the dynamics and molecular interactions between reactive intermediates and the solvent molecules at the interface to aid in optimizing the polymerization process. The molecular dynamics (MD) simulations and their experimental validation revealed the molecular interactions between the oligomeric/polymeric units of pyrrole and solvent molecules at the interface of chloroform and water. We focus on the polymer size and charge-to-size ratio in governing the confinement, interfacial coverage, and morphology during polypyrrole (PPy) formation under varying oxidant concentrations. The present results reveal that the charge-to-size ratio dictates the hydrophobic–amphiphilic–hydrophilic transition of PPy, which in turn controls the adsorption of the oligomers at the water–chloroform interface. Morphological characterizations such as FESEM, AFM, and HRTEM confirmed that at intermediate concentrations of oxidant, ammonium persulfate (APS), corresponding to the optimum charge-to-size ratio, well-defined two-dimensional PPy sheets form at the interface. The interfacial tension, density profiles, electrostatic potential, and hydrogen bonding interactions of reactive intermediates and the orientation of polymer units at the water–chloroform interface affirm the importance of the molecular interactions in controlling the *in situ* generation of conducting polymers at the L–L interface. The combined experimental and theoretical studies give profound insight into the mechanism of *in situ* interfacial polymerization and lay a foundation for controlled design of multifunctional polymer hybrids.

Received 14th July 2025,
Accepted 8th October 2025

DOI: 10.1039/d5lf00194c

rsc.li/RSCApplInter

1. Introduction

Ion transfer across the interface between two immiscible liquids is of great practical interest in areas like surface catalysis,[1] drug delivery,[2] food processing, oil-recovery,[3,4] electro-optics,[5] *etc.*[6] In particular, the thickness of such interfaces typically ranges from few angstroms to a few nanometers, creating a highly confined region where electron as well as mass transfer takes place that can be altered relative to the bulk environments.[7,8] Within this ultrathin region, the interfacial environment is governed by an interplay of intermolecular forces, including electrostatic interactions,[9,10] π–π interactions,[11] dipole–dipole interactions,[12] and H-bonding.[13] The forces collectively facilitate the spontaneous self-assembly of a variety of functional materials, such as nanoparticles,[14] surfactants,[15] polymers,[16,17] *etc.*, at the liquid–liquid interface. The driving force for the self-assembly at these interfaces is primarily the minimization of interfacial free energy/interfacial tension.[18] The confinement of the nanomaterials at the interface is determined by their amphiphilic character, particularly the balance between hydrophobic and hydrophilic segments.[19] By localizing at the interface, these amphiphilic or surface-active species reduce the interfacial tension, thereby stabilizing the interface itself.[20] Thus, the liquid–liquid interface represents an effective method for modulating the morphology of materials to achieve nanometer-sized two-dimensional (2D) films.[21]

Numerous experimental and computational studies have focused on the interfacial behavior of materials such as nanocrystals,[22,23] polymers[21] and their enzyme complexes,[24] proteins,[3] *etc.*, at the liquid–liquid interface, particularly at the water–chloroform interface due to the small molecular size, hydrophobicity and polar nature of chloroform. Among these

[a] *Department of Chemistry, National Institute of Technology Calicut, Calicut-673601, Kerala, India. E-mail: minimol@nitc.ac.in*
[b] *Department of Physics, National Institute of Technology Calicut, Calicut-673601, Kerala, India. E-mail: pnbala@nitc.ac.in*

nanomaterials, conductive polymers are of particular interest due to the conjugated π-electron systems present, which impart unique electronic properties relevant to smart electronics applications.[25,26] Notably, polypyrrole (PPy) has emerged as one of the most extensively studied conductive polymers owing to its low cost, synthetic accessibility, distinct redox properties, high electrical conductivity, and good environmental stability.[27,28] Due to their unique characteristics, PPy nanomaterials hold significant potential across various fields, including energy storage[29,30] such as batteries[31] and super capacitors[32] as well as in the medicinal field, such as sensors[33] and drug delivery,[34] flexible electronic devices,[35] and wearable electronics.[36] The construction of well-defined polymer architecture of polypyrrole materials into different nanostructures such as nanowires,[37] nanotubes,[36] nanosheets,[27] and nanoparticles[38] leads to overall performance enhancement in terms of their electronic conductivity, optical response, and microbial resistance. The significance of the liquid–liquid interface in this context lies in its unique ability to enable controlled, stimuli-responsive self-assembly processes to facilitate the morphology tuning of nanostructures. As reported previously, the physicochemical tuning of PPy polymers at the water–chloroform interface through *in situ* generation of metals, metal oxides, and doped metal oxides using various oxidants has been explored experimentally. However, systematic computational investigations into the morphology evolution of conducting polymers at the liquid–liquid interface are barely reported.

Molecular dynamics (MD) simulations offer valuable insights into molecular orientations and interactions governing the interfacial behavior of water and organic molecules of liquid–liquid interfaces and those featuring nanoparticles on a molecular scale.[39] Building on the foundational understanding of structural organization at the interface, the scope of MD simulation has been expanded to more complex interfacial systems involving nanoparticles,[14,40] surfactants,[15] and polyelectrolytes.[16,19,41] In particular, atomistic MD simulations of polyelectrolytes at the liquid–liquid interface have demonstrated that factors such as molecular concentration,[19] charge-to-size ratio, tacticity,[41] and spatial charge distribution[42] play a significant role in determining their adsorption characteristics, conformational behavior, and interfacial confinement. In addition, these parameters also influence key interfacial properties such as interfacial thickness, interfacial tension, and electrostatic interactions, especially in the presence of functional nanomaterials. Despite these advancements, a systematic understanding of how oligomeric properties, specifically chain length and charge, affect adsorption–desorption dynamics at liquid–liquid interfaces remains elusive. To date, there have been limited investigations, both experimentally and theoretically, into how such molecular features influence confinement behaviour and interfacial stabilization.

In the present study, we aim to bridge the knowledge gap by exploring the adsorption–desorption behavior of PPy oligomers at a water–chloroform interface under varying concentrations of ammonium persulfate (APS), a commonly used oxidizing agent. To achieve this, we adopt a dual-faceted approach by integrating molecular dynamics simulations with experimental characterization. The study is initiated with atomistic MD simulations to gain a molecular-level understanding of how parameters such as oligomer chain length and charge distribution influence the structural and dynamic behavior of PPy at the liquid–liquid interface. In particular, we investigate how these molecular features modulate key interfacial properties, including interfacial tension, electrostatic potential distribution, and H-bonding. The computational findings form the basis for subsequent experimental validation. Experimentally, we synthesize PPy oligomers at the water–chloroform interface by *in situ* interfacial polymerization under varying APS concentrations and analyze their morphology and assembly behavior using appropriate characterization techniques. This combined computational–experimental methodology provides a comprehensive framework for understanding the physicochemical behavior of conductive oligomers at liquid–liquid interfaces.

2. Computational and experimental section

2.1 Computational methodology

All molecular dynamics (MD) simulations were conducted using the GROMACS 2022.3 version,[43] and further visualization and structural analysis were carried out using visual molecular dynamics (VMD) software.[44] The force field parameters were based on the optimized potentials for liquid simulations all-atom (OPLS-AA) force field.[45] A combination of Coulomb interaction and Lennard Jones (LJ) force potentials with a cut-off distance of 1.4 nm is applied to represent short-range non-bonded interactions.[46] Long-range electrostatic interactions were calculated using particle-mesh Ewald (PME) methods.[47] Prior to the production run, initial structure relaxation was achieved through energy minimization using the steepest descent algorithm to eliminate any unfavorable steric contacts or high-energy configurations.[48] The minimization was followed by equilibration stages conducted under constant volume and temperature (NVT) and constant pressure and temperature (NPT) ensembles. During the NVT equilibration run conducted for 5 nanoseconds (ns), the temperature of the system was maintained at 300 K using a velocity-rescaling thermostat,[49] which ensures proper canonical ensemble sampling. In the subsequent NPT equilibration phase for 16 ns, the system pressure was maintained at 1 bar using a Berendsen barostat.[50] In the production run, the Nose–Hoover thermostat was employed for refined temperature coupling to 300 K to ensure accurate thermodynamic ensemble behavior.[51] Pressure coupling of the system to 1 bar was performed isotropically using the Parrinello–Rahman method.[52] Molecular dynamics (MD) simulations were performed for 100 ns for each system. Periodic boundary conditions were applied in all directions, and three parallel runs were performed to improve statistical reliability. The last 5 ns of each trajectory were taken out for

data processing. A leap-frog integrator was used to update particle positions and velocities at each time step of 2 fs,[53] and the LINCS algorithm was applied to ensure precise bond lengths.[54] To investigate the role of chain length and charge, PPy oligomers with 1, 2, 3, 4, 5, 10, and 15 repeating units (RU) were employed. To differentiate the effects of electrostatic interactions on the adsorption–desorption dynamics of PPy chains at the interface, each system is further classified by the total positive charge assigned to individual oligomeric (PPy) chains. A total charge of +1, +2, and +3 was assigned to all chains, except 1RU, and except 1 & 2RU, respectively. Each system was simulated using a box containing 50 PPy chains randomly distributed in $CHCl_3$ with an identical number of RUs and uniform charge distribution in all pyrrole chains; therefore, each simulation box represents a unique combination of pyrrole chain length and charge. This approach resulted in a total of 18 distinct systems, each containing a homogeneous population of PPy oligomers with specific structural and electrostatic properties. To maintain charge neutrality, a corresponding number of sulfate (SO_4^{2-}) counter ions were randomly added to the aqueous phase in each system. The design provided 18 distinct systems, each representing a unique combination of PPy chain length and charge.

2.2 Chemicals and reagents

Pyrrole (Sigma Aldrich, 109-97-7, 98%), ammonium persulfate (APS) (Sigma-Aldrich, 7727-54-0, 98%), and chloroform (Thermo Fisher Scientific India, 67-66-3, 99.5%) were used as received. Deionized water (ELGA Pure lab Quest UV, 18.2 MΩ), was employed throughout the synthesis.

2.3 Interfacial synthesis of PPy at the water–chloroform interface and characterization

To verify the influence of ionic charges on the polymerization kinetics and morphology of the PPy, interfacial polymerization of pyrrole was conducted at the interface of water and chloroform under ambient temperature–pressure conditions. In this method, the pyrrole monomer in chloroform and the oxidant ammonium persulfate in the aqueous phase were allowed to react at the water–chloroform interface for a duration of 2 hours and 45 minutes, devoid of agitation or stirring to facilitate the self-assembly of polymeric products at the interface. The influence of ionic charges during the reaction was controlled by varying five different concentrations of APS (9.75×10^{-3} to 312×10^{-3} millimoles) while maintaining a constant concentration of pyrrole monomer (731×10^{-3} millimoles). The experimental parameters, such as concentrations of reactants, volume of solvents, and product codes, are tabulated in Table S1. The final products were filtered, dried under ambient temperature–pressure conditions, and redispersed in water for further characterization.

The morphology of the products was analyzed using field emission scanning electron (FE-SEM) and high-resolution transmission electron (HR-TEM) microscopy and the topographical information was obtained using contact mode atomic force microscopy (AFM). The adsorption and desorption of reactants, intermediates, and products at the interface during the polymerization were systematically investigated using UV-visible spectroscopy (Shimadzu UV-2600 spectrometer) at different time intervals. Matrix-assisted laser desorption/ionization time-of-flight mass spectrometry (MALDI-TOF MS) was performed using a Bruker Autoflex max LRF instrument to determine the molecular weight of PPy and estimate the number of monomer units present.

3. Results and discussion

The interfacial properties of the pure water–chloroform system and the molecular interactions of polymeric chains at the water–chloroform interface were investigated using MD simulations. Fig. 1a represents a double interface box with dimensions 11 nm × 11 nm × 22 nm, which then reduced to 10.93 nm × 10.93 nm × 21.86 nm after 20 ns of MD simulation. To examine and compare the physical properties, the volume, the number of molecules, the density of each phase, and the resulting interfacial tension were simulated using two different water models (simple point charge – SPC, and extended simple point charge – SPC/E models).[12,55] As shown in Fig. 1b, simulations of pure water–chloroform systems yielded an interfacial tension value of 28.18 mN m^{-1} for the SPC–$CHCl_3$ system and 33.75 mN m^{-1} for the SPC/E–$CHCl_3$ system. It can be observed that the interfacial tension from the SPC model was closer to the experimental value of 29.7 mN m^{-1}.[56] Furthermore, the densities of aqueous and organic phases in both systems (SPC–$CHCl_3$ and SPC/E–$CHCl_3$) are in agreement with the experimental values of water and $CHCl_3$, 1000 kg m^{-3} and 1489 kg m^{-3}, respectively.[57] Density profiles of $CHCl_3$, SPC, and SPC/E were averaged over the last 5 ns of the 20 ns sample run and are shown in Fig. 1c. Consequently, the SPC model was selected for subsequent simulations in combination with the OPLS-AA force field for the other molecules, and all systems were constructed in a double interface configuration.

We investigate the morphology and adsorption–desorption behavior of PPy chains of different sizes and charges by simulating these chains in the SPC–$CHCl_3$ system. The generation of the polaronic structure of PPy during polymerization is schematically represented in Fig. S1. Fig. 2 represents the snapshots of the SPC–$CHCl_3$ system containing PPy oligomers as described in the system setup of the Computational methodology section. This design enabled a controlled investigation into how chain length and charge of PPy chains independently or jointly influence the dynamics of these polymer systems at the liquid–liquid interface.

The PPy chains, initially placed in the organic phase, were mass transferred to the aqueous phase, and/or confined at the interface based on the chain length and total charge on PPy as summarized in Fig. 2. Fig. 2a and b illustrate the behavior of short-chain PPy oligomers with one and two repeating units (1 and 2RU). Notably, 1RU exhibits significant migration towards the aqueous phase, likely due to its high

(a)

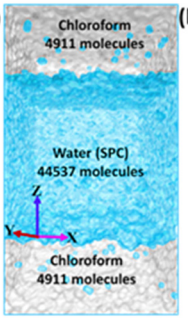

(b)

Sl. No	Parameters	Water (SPC)/ $CHCl_3$		Water (SPC/E)/ $CHCl_3$	
		Water (SPC)	$CHCl_3$	Water (SPC/E)	$CHCl_3$
1.	Volume of box (nm^3)	1306.91	1295.03	1306.91	1295.03
2.	Number of molecules	44537	9822	44537	9822
3.	Density (Kg/m^3)	961.44	1593.95	975.10	1627.81
4.	Z (nm)	21.86		21.86	
5.	Interfacial tension (mN/m)	28.18		33.75	

(c)

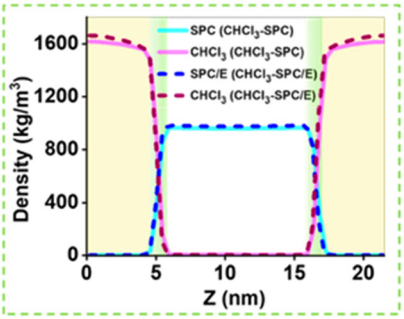

Fig. 1 (a) Water–chloroform double interface box with dimensions 10.93 nm × 10.93 nm × 21.86 nm, grey color indicates chloroform molecules and cyan color indicates water molecules. (b) The table contains details such as volume, number of molecules, the density of each phase, and the resulting interfacial tension simulated using different water models. (c) Density profiles of $CHCl_3$, SPC, and SPC/E averaged over the last 5 ns of the 20 ns sample run in both systems (SPC–$CHCl_3$ and SPC/E–$CHCl_3$).

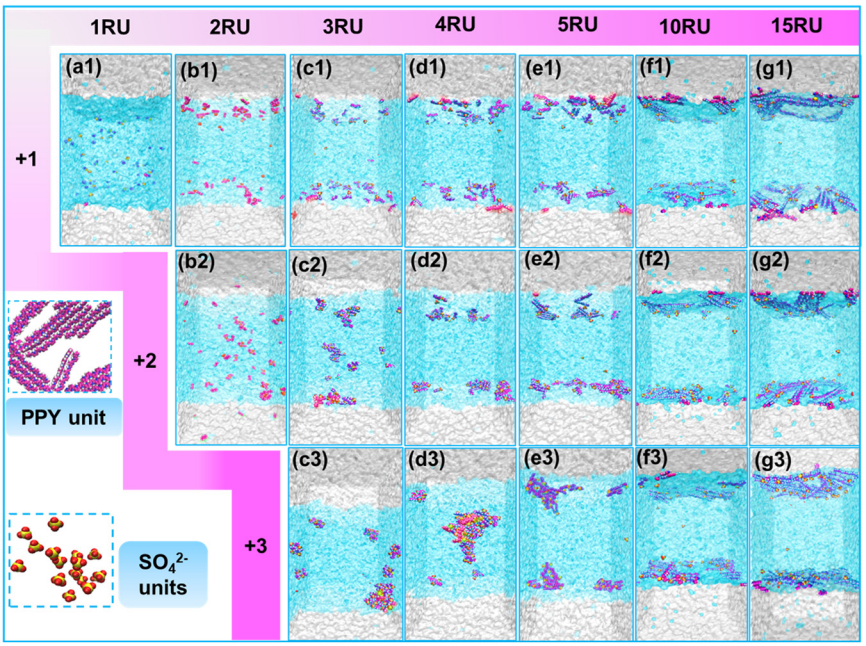

Fig. 2 Snapshots of SPC–$CHCl_3$ containing pyrrole repeating units after 100 ns of MD simulation for (a1) 1RU, (b1 and b2) 2RU, (c1–c3) 3RU, (d1–d3) 4RU, (e1–e3) 5RU, (f1–f3) 10RU, and (g1–g3) 15RU. The first, second, and third rows represent corresponding +1, +2, and +3 charges, respectively, on each PPy chain. The schematic illustrations of PPy chains and SO_4^{2-} ions are shown in the inset.

charge-to-mass ratio-induced hydrophilicity (Fig. 2a). For 2RU with +1 charge (Fig. 2b1), PPy chains are majorly confined at the interface, however, 2RU with +2 charge (Fig. 2b2) exhibited a complete distribution of PPy chains in the aqueous phase. As we move from 3RU to 5RU (Fig. 2c–e), the interfacial confinement is predominantly observed for the PPy chains with +1 charge, whereas an increase in total charge on the polymer chain helps in the distribution of the products in the aqueous phase (Fig. 2c and d). However, the 5RU oligomer shows complete confinement at the interface for charge states of +1 and +2 (Fig. 2e). For the +3 charge, although confinement is still evident, the oligomers tend to form clusters rather than spread uniformly across the interface. Some of these clusters even orient deeper towards the aqueous phase, implying the beginning of a transition from interfacial confinement to aqueous phase migration, as a result of high charge density on the PPy chains. The long-chain oligomers 10RU and 15RU (Fig. 2f and g) exhibit robust confinement at the water–chloroform interface across all studied charge states (+1, +2, and +3).

To better understand how PPy oligomers are confined at the water–chloroform interface, mass density profiles were examined for each system. These profiles quantitatively reveal the spatial distribution of PPy chains and counter ions (SO_4^{2-}) and chain length at the interface as well as in the bulk phases. The results presented in Fig. 3 and 4 depict the mass density profiles for varying charge densities and chain lengths. Fig. 3a–d represents the mass density profiles of PPy chains with higher charge density per RU such as 1RU (+1 charge), 2RU (+2 charge), 3RU (+2 and +3 charges), and 4RU

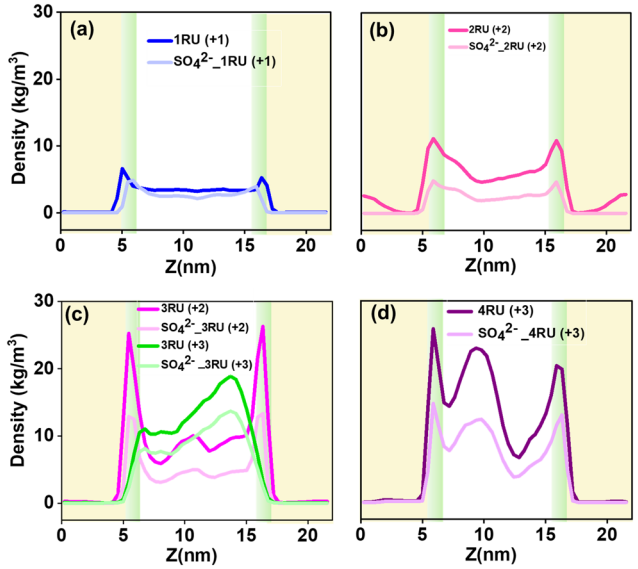

Fig. 3 Mass density profiles of PPy chains with higher charge density per RU. (a) 1RU (+1 charge), (b) 2RU (+2 charge), (c) 3RU (+2 and +3 charges), and (d) 4RU (+3 charge).

(+3 charge). PPy chains with higher charge density tend to migrate towards the aqueous phase, mainly due to electrostatic interactions with the polar solvent. Fig. 3a demonstrates the mass density profile of 1RU with a +1 charge, highlighting the significant presence of the species in the aqueous phase due to the migration of high-charge-density PPy units to the aqueous phase. Fig. 3b depicts the mass density of 2RU with +2 charge, with peak intensity surpassing that of 1RU attributed to the increase in oligomeric chain length (total mass of PPy chain). Fig. 3c shows the density profiles for 3RU with +2 and +3 charges. The +2 charged species exhibit minimal interfacial confinement and a noticeable shift in density towards the aqueous phase, suggesting limited stabilization at the interface and enhanced distribution of PPy chains in water. On the other hand, for the +3 charged species the density distribution is even more dispersed within the aqueous phase, with almost no interfacial confinement. This distribution pattern of 3RU indicates that an increase in charge per RU considerably decreases the affinity of PPy chains towards the hydrophobic chloroform, favoring its movement into the aqueous phase. Finally, Fig. 3d illustrates the density profile for 4RU with +3 charge, which displays high intensity corresponding to PPy chains dispersed in the aqueous phase. The nature of density plots further confirms that highly charged PPy chains (particularly at +3 per RU) are unable to maintain stable interfacial confinement due to the dominant electrostatic interaction with water.

Fig. 4 illustrates the mass density profiles of lower charge density of PPy chains of 2RU & 3RU (+1 charge), 4RU (+1 and +2 charge), 5RU, 10RU, and 15RU (+1, +2 and +3 charges). The peak height of the density profile at the interface correlates with the increase in chain length, particularly for PPy with repeating units 10 and 15. In contrast to Fig. 3, the density profiles of Fig. 4 feature sharp and narrow peaks at the interface corresponding to PPy and SO_4^{2-} ions, suggesting the absolute localization and planar confinement of the oligomers at the narrow interface of water and chloroform. Fig. 4a details the density plot of 2RU, each chain bearing a +1 charge, and the peak intensity at the interface is very low due to its small size. In this configuration, the PPy chain exhibits major confinement at the interface. Oppositely, in the case of 3RU (+1 charge), 4RU (+1 and +2 charge), and

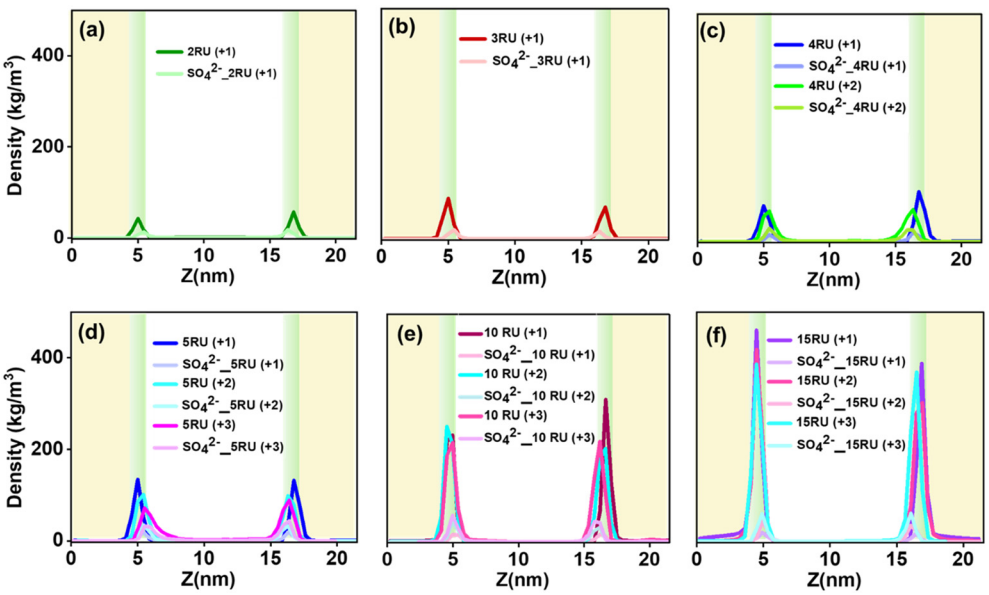

Fig. 4 Mass density profiles of PPy chains with lower charge density per RU. (a) 2RU (+1 charge), (b) 3RU (+1 charge), (c) 4RU (+1 and +2 charges), (d) 5RU (+1, +2 and +3 charge), (e) 10RU (+1, +2 and +3 charge), and (f) 15RU (+1, +2 and +3 charge).

5RU (+1 and +2 charge), Fig. 4b–d show sharp peaks at the interface which confirms the complete confinement of PPy chains at the interface. Although peaks corresponding to density profiles of 5RU (+3 charge) of the PPy oligomer appear to be confined at the interface, they are slightly broadened towards the aqueous phase compared to 5RU with +1 and +2 charges. On comparing the mass density profiles of 3RU, 4RU, and 5RU PPy chains, it can be concluded that the PPy chains exhibit charge density-dependent confinement at the interface. For longer chains of 10RU and 15RU (Fig. 4e and f respectively), sharp and narrow peaks are consistently observed regardless of the charge per RU, where the designated charges are +1, +2, and +3. As depicted from the mass density profiles of SO_4^{2-} counter ions in Fig. 3 and 4, the counter ions are also confined at the interface. The spontaneous electrostatic association of counter ions with the positively charged NH_2^+ terminal of PPy chains makes them more hydrophilic in nature.

The preferential distribution and the nature of self-assembly of PPy chains and the solvent accessible surface area (SASA) at the interface were analyzed from the top-down (*z*-axis) view of the interface of simulated systems (Fig. 5). For this particular study, the authors have selected only the samples in which the PPy chains are majorly or completely adsorbed at the interface. In Fig. 5a–f, the first, second, and third rows represent the PPy chains with total charges, +1, +2, and +3, respectively. On comparing the PPy chains with the same total charges, for example, PPy chains of 2, 3, 4, 5, 10, and 15RUs with +1 charge (left to right in the first row of Fig. 5), the surface coverage increases with an increase in RU per chain. Moreover, as shown in Fig. 5e and f, 10RU and 15RU have more planar sheet-like structures where individual oligomer chains lie parallel and stack side-by-side. In contrast, when the total charge increases for fixed chain length PPy (+1 and +2 for 4RU and +1 to +3 for 5RU), a transition from planar stacking to agglomeration of PPy chains is observed in Fig. 5c and d. In longer chains (10 and 15 RU), the stacked 2D sheets-like nature persists even at higher charge densities, although some lateral dispersion is observed as the charge increases. To support this observation, the 2D density maps of the PPy chains at the interface are also provided in Fig. S2. Based on these observations, it can be concluded that the charge-induced agglomeration is more pronounced for medium-length than for longer PPy chains, leading to a morphology tuning from agglomerated clusters to two-dimensional sheets. Apart from this, the surface coverage of PPy chains was quantified using the solvent accessible-surface area (SASA), by the Connolly method which reflects the extent of oligomer exposure to the surrounding medium and contributes to the understanding of interfacial stabilization and adsorption mechanism.[58] As shown in Fig. 5g, the SASA decreases with an increase in the total charge for medium chain length (3RU, 4RU, and 5RU), reflecting increased agglomeration and reduced interfacial spread. In contrast, for long-chain PPy, the SASA does not vary significantly. However, as the chain length increases (10 and 15RUs), the SASA more or less remains the same with an increase in total charge, indicating more dispersed and compact stacking of PPy chains at the interface.

The influence of the adsorbed PPy chains on minimizing the interfacial tension (IFT) and stabilization of a high-energy water–chloroform interface was compared with that of a pure water–chloroform system. The interfacial tension (γ) between the aqueous and organic phases, both in the presence and

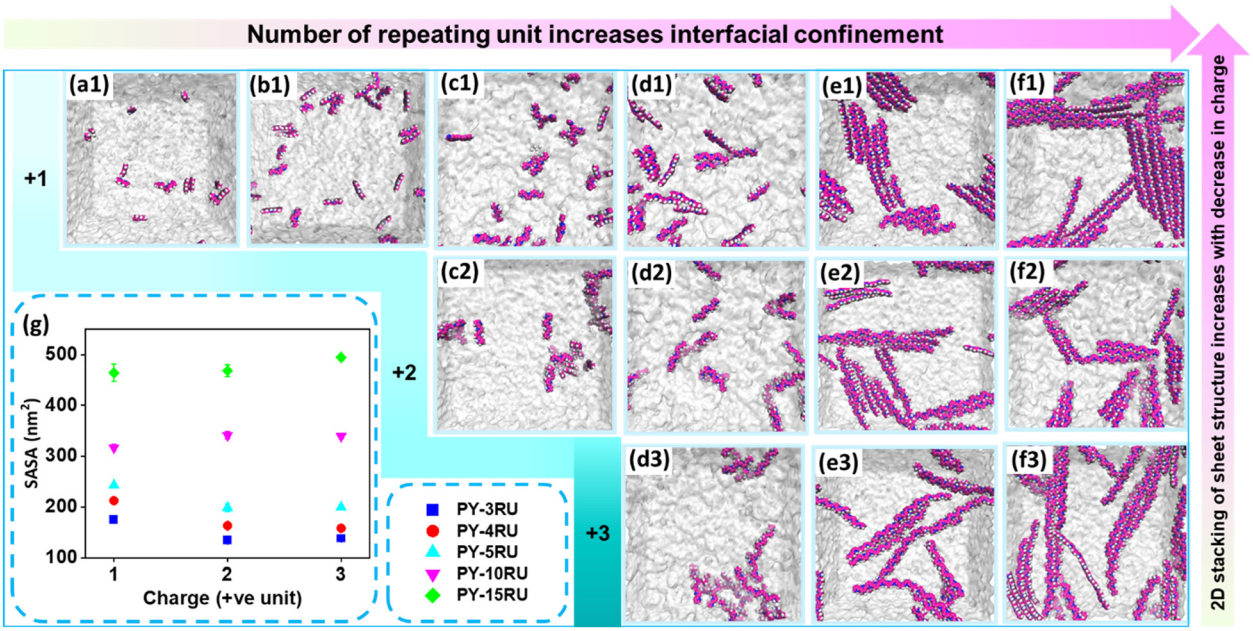

Fig. 5 Snapshots of interfacial coverage at the SPC–$CHCl_3$ interface for PPy chains of (a1) 2RU, (b1) 3RU, (c1 and c2) 4RU, (d1–d3) 5RU, (e1–e3) 10RU, and (f1–f3) 15RU. The first, second, and third rows represent corresponding +1, +2, and +3 charges, respectively, on the corresponding PPy chain. (g) Solvent accessible surface area (SASA) of PPy chains as a function of total charge per chain.

absence of PPy oligomers, was computed using the mechanical definition derived from pressure tensor components:[59]

$$\gamma = \frac{L_z}{2}\left(p_z - \frac{p_x + p_y}{2}\right) \quad (1)$$

where L_z is the length of the simulation box along the z-axis (direction perpendicular to the interface), p_z is the normal pressure component, and p_x and p_y are the tangential pressure components. A factor of 1/2 accounts for the presence of two interfaces arising from periodic boundary conditions applied in the z-dimension. The interfacial tensions of all the systems calculated in the last 5 ns of MD simulations are summarised in Fig. 6a. As mentioned earlier, the interfacial tension of pure SPC–$CHCl_3$ (γ_0) was 28.18 mN m^{-1}. Regarding the IFT in the case of medium-length PPy chains (3RU, 4RU, and 5 RU), an increase in IFT with an increase in total charge (+1 to +3) was observed. However, the maximum IFT observed for these systems was 28.29 mN m^{-1} for 3RU with a +3 charge, which is almost similar to the IFT of pure SPC–$CHCl_3$. In contrast to the behavior observed for medium-chains, long-chain PPy (10RU and 15RU) shows a decrease in IFT (γ) with an increase in total charge. The lowest IFT values for 10 RU and 15 RU at a total charge of +3 are 26.7 mN m^{-1} and 24.8 mN m^{-1}, respectively. As reported earlier, the decrease in IFT is attributed to the increased stabilization of the water–chloroform interface as a result of the adsorbed nanostructures.[23,33] The illustrations in Fig. 2 and 5 additionally emphasize the adsorption of nanostructures at the interface. Therefore, it further affirms that the adsorption of PPy chains at the interface decreases IFT, whereas the agglomeration/distribution of PPy chains in the aqueous phase resulted in IFT values similar to that of the pure SPC–$CHCl_3$ system.

Molecular ordering and polarization of solvent molecules as a result of the adsorption/desorption of PPy chains were investigated using the electrostatic potential across the water–chloroform interface as shown in Fig. 6b and c. The electric potential difference across the interface was evaluated by performing a double integral of the charge distribution of the system in z-direction using the Poisson equation in its integrated form:[60]

$$\psi(z) - \psi(0) = -\int_0^z dz' \int_0^{z'} dz'' \frac{\rho_e(z'')}{\varepsilon_0} \quad (2)$$

In this expression, $\psi(z)$ and $\psi(0)$ are the electrostatic potentials at position z, and at the reference point z = 0, respectively. ε_0 is the vacuum permittivity, and $\rho_e(z)$ is the spatially resolved charge density along the z-direction. For the pure SPC–$CHCl_3$ interface, the interface electrostatic potential was calculated to be −624 mV, which is consistent with the theoretical value reported.[61] The electrostatic potential becomes more negative at the interface by the incorporation of PPy oligomers. We notice that there is a change in the shape of the electrostatic potential, as we move to +3 charge configurations, which may be an artefact of the box size we have chosen. In these contexts, based on the shape of the potential well, they are categorized into two, electrostatic potential trends exhibited by PPy with lower total charge (+1 and +2) as shown in Fig. 6b and PPy with higher total charge (+3 charge) represented in Fig. 6c. For PPy chains with +1 and +2 charge, as the number of repeating units increases, the electrostatic potential minimum at the interface becomes more negative. Among these systems, 15RU with +2 charge exhibits the lowest electrostatic potential, suggesting that long chains with moderate charge

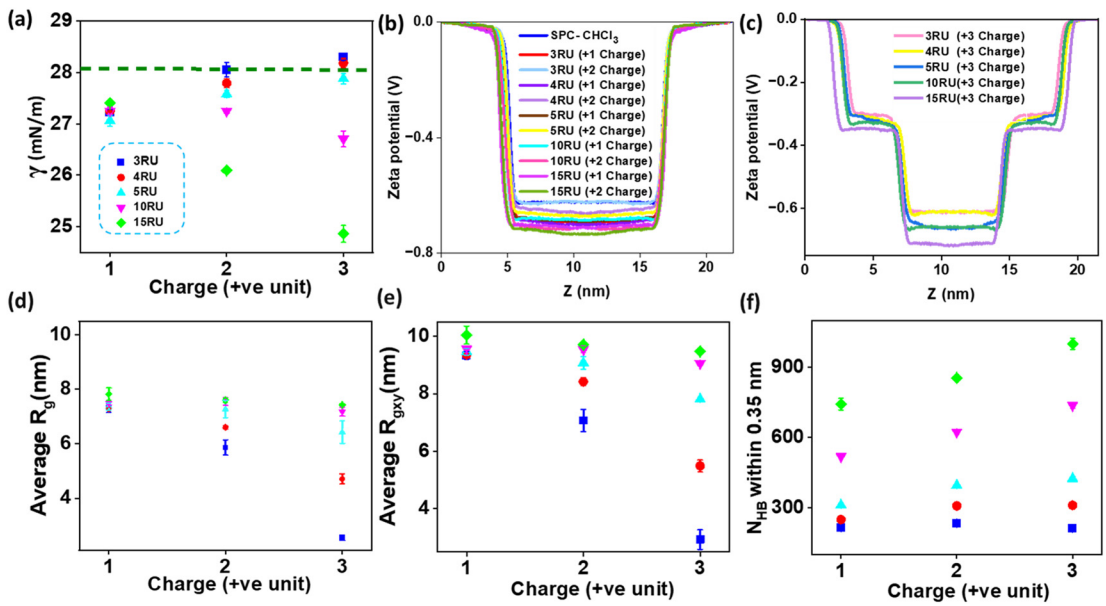

Fig. 6 (a) Interfacial tension, (b) electrostatic potential of PPy chains with charge +1 and +2 per chain, (c) electrostatic potential of PPy chains with charge +3 per chain, (d) average radius of gyration R_g, (e) average radius of gyration along the xy plane R_{gxy} and (f) number of H-bonds within 0.35 nm of PPy chains.

induce the strongest polarization on solvent molecules close to the interface. This may be due to the extended surface contact and the stronger electrostatic field generated by the longer chains. As shown in Fig. 6c, the potential profiles exhibit a step-wise well structure for +3 charge, which is notably different from chains with low charge. Additionally, the charge distribution arising from the solvent–polymer interactions is shown in Fig. S3. For PPy chains with +1 and +2 charges, the charge is more concentrated near the interface giving rise to sharper charge density peaks near the interface (Fig. S3a). On the other hand, for PPy chains with total charge +3, charge multiple charge zones (Fig. S3b) are formed along the box that may contribute to the distinct structure of the electrostatic well for +3 charge.

Moreover, the radius of gyration R_g provides insight into the conformational behavior of PPy chains during polymerization. The overall spatial extent of the oligomers (R_g) and the spread of the oligomers within the interfacial 2D plane (R_{gxy}) are shown in Fig. 6d and e, respectively. The plots of both R_g and R_{gxy} reveal a clear tendency of aggregation among the oligomers for medium chains (3RU, 4RU, and 5RU) as the total charge increases. The radius of gyration processed from the last 5 ns of each trajectory is represented in Fig. S4. Notably for medium chains, an increase in charge density drives conformational transitions from 2D arrangement to aggregated clusters, implying the dominant role of electrostatic interactions over chain length in determining the interfacial confinement. In contrast to medium chain length, longer chains (10RU and 15RU) have almost constant R_g values, and tend to adopt a more spread-out conformation at the interface, independent of the total charge on the chains. Furthermore, to quantitatively investigate the role of polymer–solvent interaction in deciding the confinement at the interface/distribution to the solvent phase, H-bonding interactions with surrounding water molecules were analyzed. The distance and angular criteria for hydrogen bonds were defined using the standard geometric criteria corresponding to the first minimum in the donor–acceptor radial distribution function, which ensures near-linearity of the hydrogen bond.[62] The number of hydrogen bonds (N_{HB}) within 0.35 nm of PPy chains (Fig. 6f) shows an increase with an increase in total charge. The variation of N_{HB} is detailed in Fig. S5 and can be correlated with the radial distribution function (RDF) of SO_4^{2-} ions around the PPy chains as shown in Fig. S6. Moderate chain length oligomers, such as 3RU, 4RU, and 5RU, show stronger localized electrostatic interaction with SO_4^{2-} ions at higher total charges due to concentrated positive charge. This results in enhanced clustering of SO_4^{2-} ions around the PPy chains which leads to an increase in the N_{HB} value with an increase in total charge. The corresponding reduction in R_g value confirms that the oligomers are highly agglomerated and more distributed into the aqueous phase. In contrast, the delocalized charge on longer PPy (10RU and 15RU) chains leads to a lower probability of SO_4^{2-} ion accumulation in the vicinity of PPy chains as shown by the lower RDF value compared to that of medium chains. However, N_{HB} values for longer chains remain high, due to the greater number of N atoms that act as hydrogen bonding sites. Despite the high N_{HB} values, the radius of gyration remains unchanged for longer chains suggesting that these PPy chains retain 2D natured confinement and do not undergo aggregation.

MD simulation findings were further verified using experimental methods, in which the dynamics at the interface and the morphology tuning of PPy nanostructures were investigated. To elucidate the dynamics of reactive intermediates and their distribution across the interface, UV-visible absorption spectral analysis was carried out during polymerization using four different concentrations of ammonium persulfate. The samples were collected from three different regions, *i.e.*, (i) bulk aqueous phase (ii) near the water–chloroform interface and (iii) bulk organic phase every 15 minutes over a total period of 2 h and 45 minutes on each sample, *i.e.*, PPy2 to PPy5 (Table S1). The reaction dynamics of reactive intermediates were recorded using UV-visible absorbance spectroscopy for SO_4^{2-}, PPy oligomeric chains, and monomer peaks at 185 nm, 210 nm, and 240 nm, respectively, as shown in Fig. S7 and S8. As the reaction proceeds, the intensity of the monomer and oxidant decreases due to the consumption of reactants, whereas the intensity of oligomeric chains increases due to the polymerization. The UV-vis characterization of PPy1 was not included in the comparison as there is no visible product formation for this particular concentration. Fig. 7 represents the variation in the intensity of absorption for the reactive species in the bulk aqueous phase, near the water–chloroform interface, and bulk organic phase. Fig. 7a represents the temporal evolution of peak intensity for the SO_4^{2-} ions in the aqueous phase and at the interface for the samples PPy2 and PPy3, in which the APS concentration is low. The concentration of SO_4^{2-} ions decreases with time, in particular, a sharp decrease in concentration was observed within the first 1 hour, however, a very slow decrement was subsequently seen. At the same time, the concentration of SO_4^{2-} ions increases similarly at the interface, indicating the consumption of APS from the aqueous phase and generation of the SO_4^{2-} ion attached oligomers at the interface. Meanwhile in the case of PPy4 and PPy5, SO_4^{2-} ions in the aqueous phase sharply decrease within 1 hour; however, the concentration increases during polymerization (Fig. 7b). Moreover, the SO_4^{2-} ion concentration at the interface increases within 1 hour and slowly decreases, indicating the fast generation of SO_4^{2-} ion attached oligomers at the interface, initially migrating to the aqueous phase due to the attachment of a higher number of SO_4^{2-} ions to the PPy chains. These experimental observations corroborate with the MD simulations, where the agglomeration and distribution of PPy chains are more prominent at higher concentrations of SO_4^{2-} ions. Fig. 7c represents the decrease in the concentration of pyrrole monomers distributed in the organic phase for all samples (PPy2 to PPy5), indicating the consumption of monomers during polymerization. The percentage depletion of pyrrole monomers was significantly higher for PPy4 and PPy5 samples, indicating enhanced monomer consumption at higher APS concentrations which in

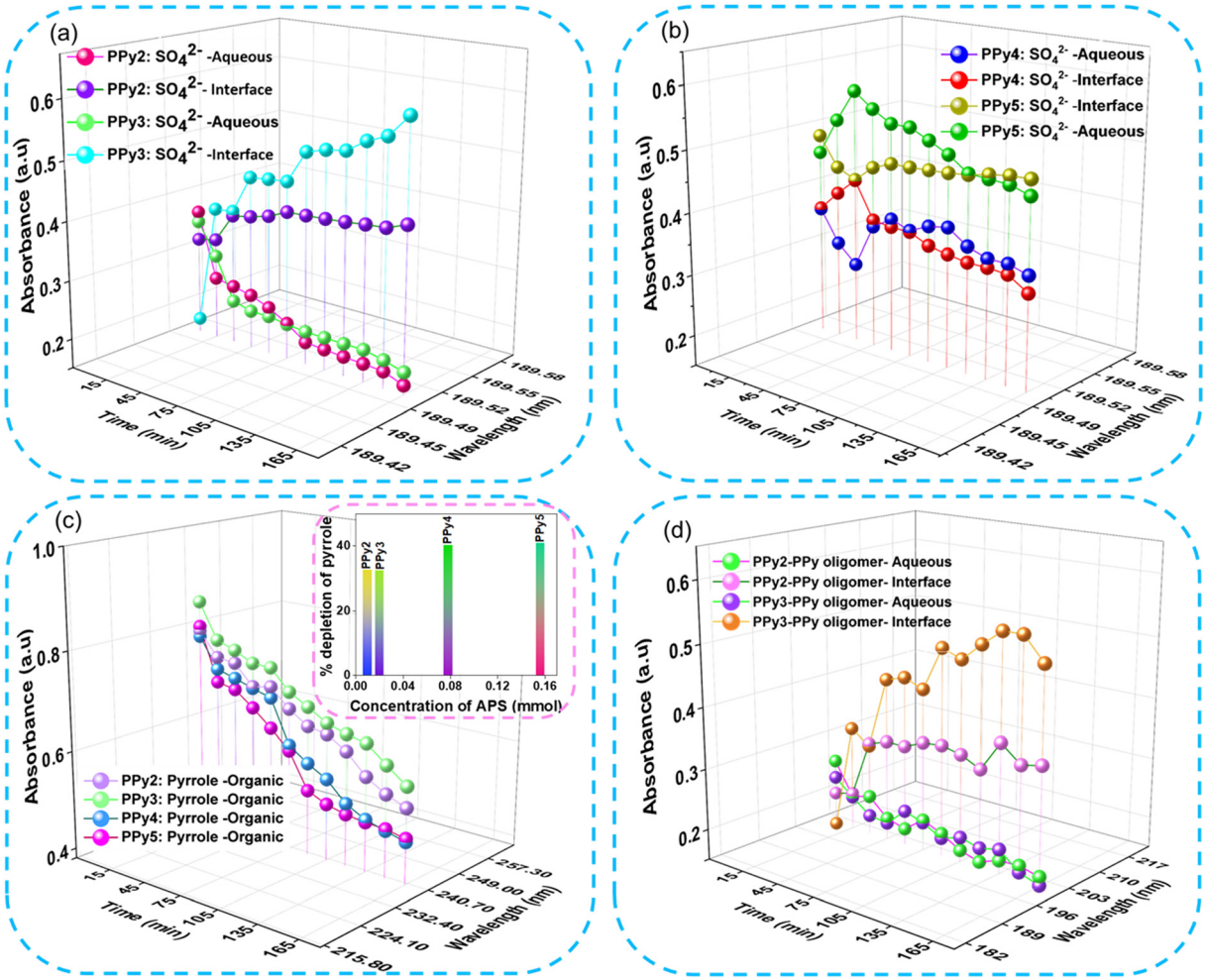

Fig. 7 Absorption peaks for SO_4^{2-} ions (a) at lower concentrations of APS (PPy2 and PPy3) in the aqueous phase, (b) in higher concentrations of APS (PPy4 and PPy5) in the aqueous phase and (c) absorption peaks of pyrrole in the organic phase for PPy2, PPy3, PPy4, and PPy5. The inset shows the depletion percentage of pyrrole monomers during the reaction. (d) The oligomeric absorbance observed in PPy2 and PPy3 was sample collected from the aqueous and interface.

turn hinders the formation of longer PPy oligomers. In contrast, slower depletion at lower APS concentrations (PPy2 and PPy3) allows sufficient availability of monomers for oligomer growth. The fair comparison between Fig. S7 and S8 proves the formation of long-chain oligomers, indicated as a broad peak closer to SO_4^{2-} ion absorption. This is further supported by Fig. 7d, where the absorbance intensity of PPy oligomers increases at the interface for PPy2 and PPy3, while it remains low or decreases at the aqueous phase with time, suggesting that PPy oligomer formation predominantly occurs at the interface under low APS concentrations.

MD simulations proved that the doping of SO_4^{2-} ions to the PPy chains plays a crucial role in regulating the migration and tuning the morphology of PPy nanostructures generated in the bisolvent systems. Hence, the impact of APS concentration on both the dynamics of interfacial polymerization and the morphology of PPy nanostructures of samples PPy1 to PPy5 is depicted in Fig. 8. The optical images of the reaction medium allowed to react for 3 hours indicate the different modes of product confinement for different APS concentrations (Fig. 8a1–e1). The nature of product generation and its distribution/confinement varies based on the APS concentrations. At the lowest APS concentration (PPy1) there was no visible product formation, while for PPy2 a very thin layer of product started to confine at the interface by 1 hour and 45 minutes of reaction. As the oxidant concentration was increased, PPy3 showed more pronounced confinement of products at the water–chloroform interface, significantly earlier, within 1 hour. Furthermore, both PPy2 and PPy3 do not extend the products to the bulk phase, possibly due to the low oxidant concentration, which reduces SO_4^{2-} ion doping and restricts the diffusion of reactive intermediates towards the bulk aqueous phase.

In contrast, at higher APS concentrations (PPy4 and PPy5), product formation becomes faster, and *in situ* generation of the product occurs within the first 30 minutes. It should be noted that the products extend beyond the water–chloroform interface, and are evenly distributed in the aqueous phase. Apart from this, the influence of APS concentration in tuning

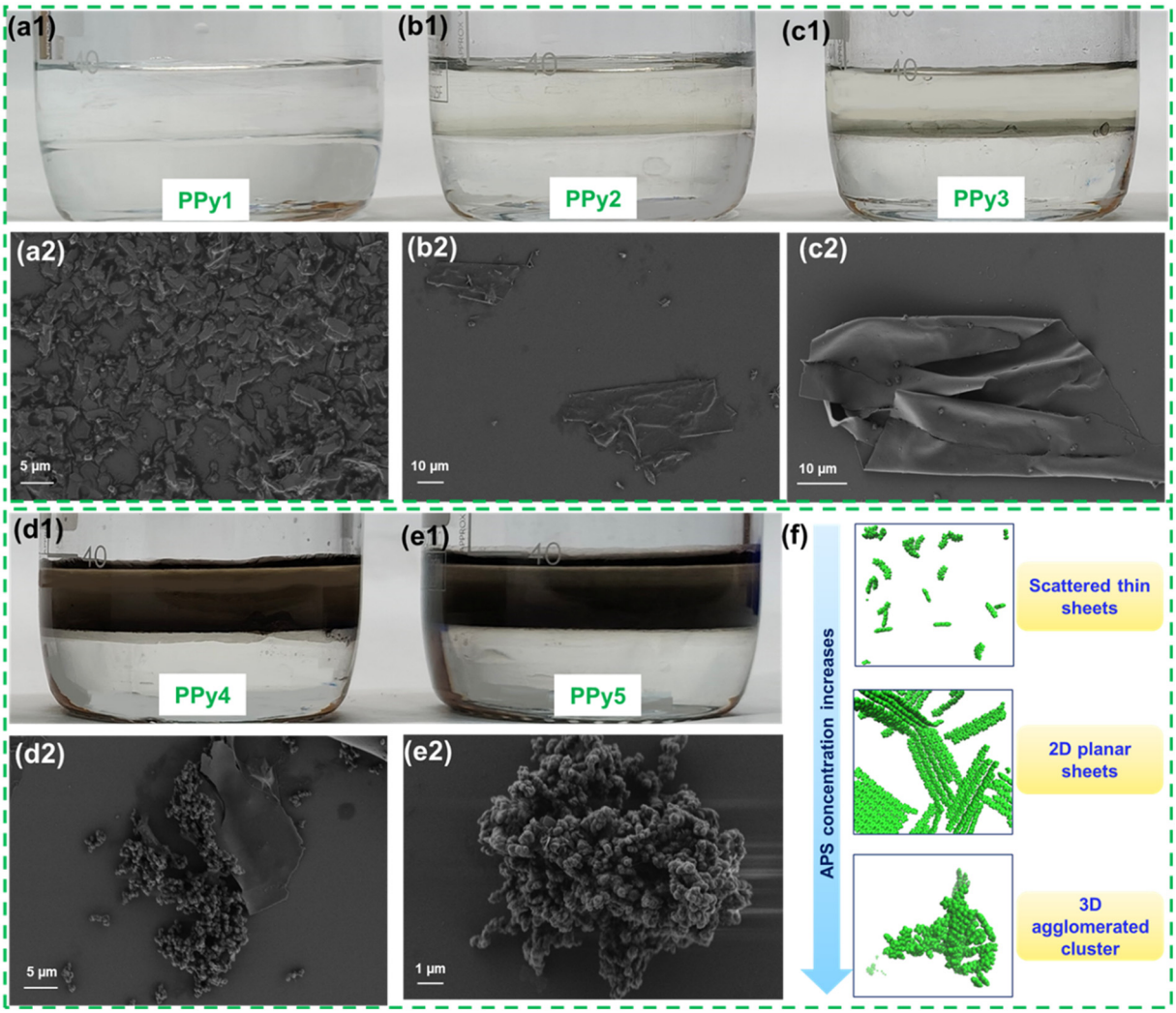

Fig. 8 (a1–e1) Optical images of the formation of PPy at the water–chloroform interface after the polymerization completion PPy1–PPy5, and (a2–e2) the corresponding FE-SEM images. (f) Illustration of the transition of product morphology from scattered thin sheets to agglomerated clusters with increasing APS concentrations.

the morphology of the PPy nanostructures was investigated with the help of high-resolution scanning electron microscopy, as shown in Fig. 8a2–e2. Interestingly, the morphology was modulated from irregularly shaped small sheets to well-defined two-dimensional PPy sheets to three-dimensional agglomerated clusters, as the concentration of APS varied from very low to medium to high concentrations. Insufficient APS concentration (PPy1) leads to minimal PPy generation, leading to irregularly shaped sheets smaller than 5 micrometers (Fig. 8a2). However, Fig. 8c2 shows well-defined two-dimensional PPy sheets formed for an intermediate concentration of APS (PPy3), and the products were stabilized at the water–chloroform interface. This suggests that the optimal concentration of APS facilitates the controlled formation of reactive intermediates that may align and stack parallel to the water–chloroform interface to form larger two-dimensional sheets. Further increase in APS concentration (PPy4) leads to the combination of sheet and globular nanostructures (Fig. 8d2). At the highest concentration of APS (PPy5), the product morphology completely changed to a three-dimensional network of globular structures (Fig. 8e2). The cluster morphology can be attributed to rapid oxidation that contributes to small agglomerated clusters with highly positive charge density. The high charge density increases hydrophilicity which leads to enhanced diffusion into the bulk aqueous phase. The experimental observations from FE-SEM at various APS concentrations agree with the theoretical predictions, as shown in Fig. 2. On comparing Fig. 8a1–c1 with that of the PPy chains with the same total charges, for example, PPy chains of 2, 3, 4, 5, 10, and 15 RUs with +1 charge (left to right in the first row of Fig. 2), the sheet nature becomes prominent with the increase in chain length. Moreover, as a result of the generation of more reactive oligomeric chains with increasing APS concentrations (PPy1–PPy3), the increase in repeating units leads to more robust films. On the other hand, the excess APS concentration (PPy4 and PPy5) provides more SO_4^{2-} ions for doping on the PPy chains in addition to the rapid oxidation of monomers, resulting in the generation of agglomerated clusters with high charge density. Theoretical analogs corresponding to this

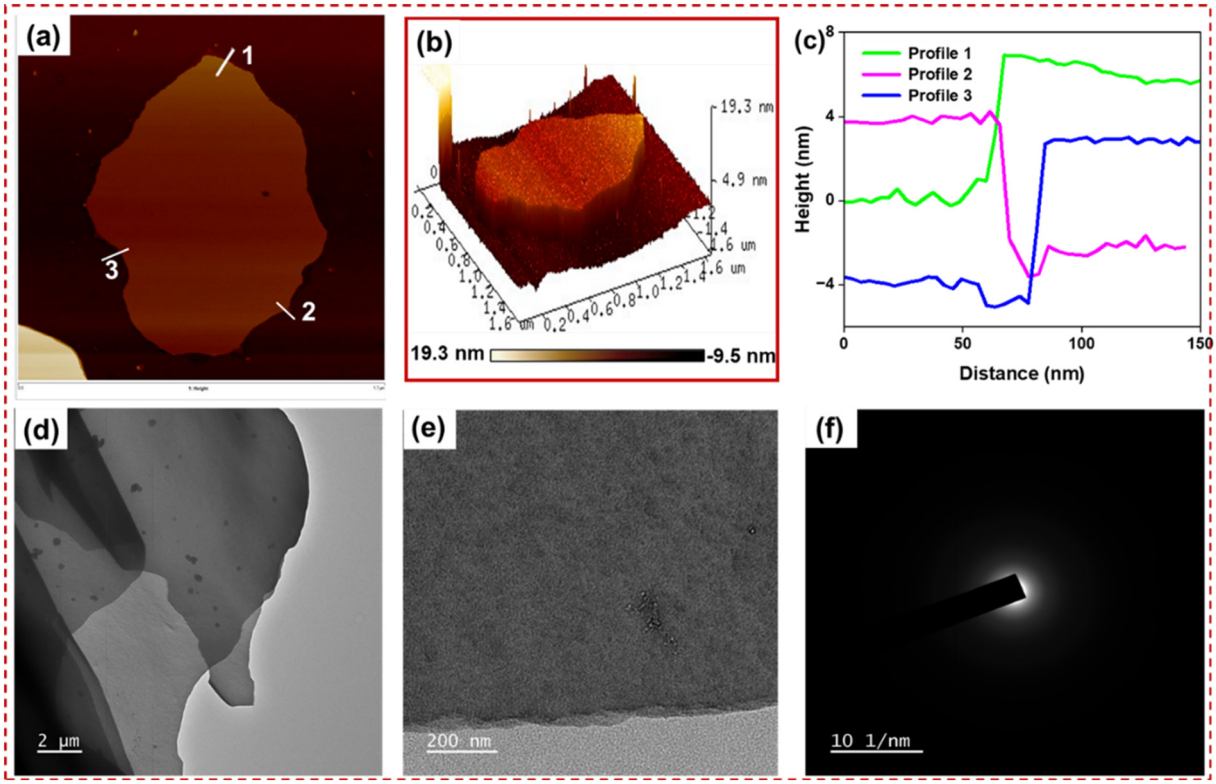

Fig. 9 AFM and HR-TEM analysis of PPy3 samples. (a) 2-D AFM image, (b) 3-D AFM image, (c) thickness plot at three different regions denoted as profile 1, 2, and 3. (d) and (e) HR-TEM image and (f) selected area diffraction pattern of the PPy3 sample.

phenomenon include moderate chains with higher charge density, such as 4RU (+3 charge) and 3RU (+2 and +3 charge density), as in Fig. 2. Fig. 8f pictorially illustrates the evolution of the morphology of PPy nanostructures as a function of APS concentration.

The high interfacial tension-induced morphologically tuned 2D nanostructures were further investigated using AFM and HR-TEM techniques to elucidate the 2D stacking behavior. For this, the products from PPy3 were selected owing to their robust 2D sheet structure. The 2D-AFM image (Fig. 9a) and 3D-AFM image (Fig. 9b) exhibited planar two-dimensional sheets with a uniform thickness throughout. Furthermore, the thickness profiling at three different regions of the film showed an approximate thickness of 6 nm, resulting from the layered packing of roughly 40 PPy chains in a single sheet (Fig. 9c). Additional AFM imaging and thickness profiling of the same sample are included in Fig. S9, further confirming the uniform morphology and thickness of the PPy3 samples. In addition, the HR-TEM analysis (Fig. 9d and e) shows two-dimensional nano-sheet structures consistent with those observed in both AFM and SEM. The selected area electron diffraction (SAED) pattern (Fig. 9f) displayed diffuse diffraction rings, affirming the characteristics of the amorphous nature of PPy sheets. Further, the molecular weight of PPy and the number of monomer units were estimated from the MALDI-TOF MS analysis of the PPy3 sample. The MALDI spectrum shows distinct peaks corresponding to PPy oligomers with chain lengths in the range of 7 to 15 repeating units, which is in agreement with PPy synthesized using chemical oxidative polymerization in a single solvent.[63]

Conclusion

An in-depth comprehension of the interfacial polymerization of polypyrrole by the integration of molecular dynamics simulations with experimental validation is explored in this work. MD simulations revealed that the charge-to-size ratio of PPy oligomers determined the region of confinement: short oligomers with higher charge density preferentially migrate to the aqueous phase, whereas oligomers with low charge density exhibit strong interfacial confinement and form two-dimensional stacked sheets. Experimentally, the charge density was controlled by varying the APS concentrations, and FESEM, AFM, and HRTEM analysis confirmed that, at intermediate APS concentrations corresponding to optimum charge to size ratio, well-defined two-dimensional PPy sheets form at the interface. Higher APS concentrations yielded agglomerated clusters in the aqueous phase, consistent with molecular dynamics predictions for highly charged short-to-medium length oligomers. Further, the reduction in interfacial tension and electrostatic potential predicted by the simulations was supported by data from UV-vis spectroscopy. The UV-vis absorption intensities of SO_4^{2-} and PPy oligomers are positively correlated with migration and confinement of PPy chains at the interface as observed in the MD simulations. It also revealed that at lower APS

concentrations (PPy2 & PPy3), SO_4^{2-} consumption and oligomer growth predominantly occur at the water–chloroform interface, while higher APS concentrations (PPy4 & PPy5) promote their migration into the aqueous phase. These trends are consistent with MD simulations, which predicted that high charge density favors migration of oligomers into the aqueous phase, whereas lower charge density promotes interfacial confinement and two-dimensional nanosheet formation. The number of hydrogen bonds and radius of gyration analyses further evidenced how electrostatic interactions govern interfacial confinement, which agrees with the experimentally observed tuning from thin nanosheets to agglomerated morphologies at higher oxidant levels. Overall, the integrated MD–experimental framework provides a consistent molecular picture: simulations supply mechanistic insights into charge-driven adsorption, confinement, and morphology, while experimental observations validate these predictions. This synergy underscores the critical role of the charge-to-size ratio of PPy chains in tuning PPy nanostructures at liquid–liquid interfaces and establishes a predictive platform for designing interfacial polymerization.

Conflicts of interest

The authors declare no conflict of interest.

Data availability

The data supporting this article have been included as part of the supplementary information (SI). See DOI: **https://doi.org/10.1039/d5lf00194c**.

Acknowledgements

The authors acknowledge DST-FIST for FE-SEM. The authors are thankful to CSIR-NIIST, Thiruvananthapuram for HRTEM-SAED analysis. Aiswarya Chandran acknowledges UGC for a fellowship grant (Grant number: 201610132765). P N Bala Subramanian acknowledges the Faculty Research Grant (FRG) 2022-24 (FRG/2022/PHY_01) by the National Institute of Technology Calicut (NITC), India. The authors thank Pro. Parameswaran Pattiyil, Department of Chemistry, National Institute of Technology Calicut for fruitful discussions. The authors also thank the Centre for Computational Modelling and Simulation (CCMS), NIT Calicut, for computational support.

References

1 Z. Chen, L. Zhou, W. Bing, Z. Zhang, Z. Li, J. Ren and X. Qu, Light Controlled Reversible Inversion of Nanophosphor-Stabilized Pickering Emulsions for Biphasic Enantioselective Biocatalysis, *J. Am. Chem. Soc.*, 2014, **136**(20), 7498–7504, DOI: **10.1021/ja503123m**.

2 D. Patra, A. Sanyal and V. M. Rotello, Colloidal Microcapsules: Self-Assembly of Nanoparticles at the Liquid-Liquid Interface, *Chem. – Asian J.*, 2010, **5**(12), 2442–2453, DOI: **10.1002/asia.201000301**.

3 B. Schnell, R. Schurhammer and G. Wipff, Distribution of Hydrophobic Ions and Their Counterions at an Aqueous Liquid-Liquid Interface: A Molecular Dynamics Investigation, *J. Phys. Chem. B*, 2004, **108**(7), 2285–2294, DOI: **10.1021/jp036896m**.

4 J. G. Lee, L. L. Larive, K. T. Valsaraj and B. Bharti, Binding of Lignin Nanoparticles at Oil-Water Interfaces: An Ecofriendly Alternative to Oil Spill Recovery, *ACS Appl. Mater. Interfaces*, 2018, **10**(49), 43282–43289, DOI: **10.1021/acsami.8b17748**.

5 Y. Montelongo, D. Sikdar, Y. Ma, A. J. S. McIntosh, L. Velleman, A. R. Kucernak, J. B. Edel and A. A. Kornyshev, Electrotunable Nanoplasmonic Liquid Mirror, *Nat. Mater.*, 2017, **16**(11), 1127–1135, DOI: **10.1038/NMAT4969**.

6 A. W. Adamson and A. P. Gast, *Physical Chemistry of Surfaces*, Wiley, 1990, p. A467.

7 M. Luo, Y. Song and L. L. Dai, Heterogeneous or Competitive Self-Assembly of Surfactants and Nanoparticles at Liquid-Liquid Interfaces, *Mol. Simul.*, 2009, **35**(10–11), 773–784, DOI: **10.1080/08927020902769851**.

8 D. Michael and I. Benjamin, Molecular Dynamics Computer Simulations of Solvation Dynamics at Liquid/Liquid Interfaces, *J. Chem. Phys.*, 2001, **114**(6), 2817–2824, DOI: **10.1063/1.1334902**.

9 T. M. Chang and L. X. Dang, Molecular Dynamics Simulations of CCl4-H2O Liquid-Liquid Interface with Polarizable Potential Models, *J. Chem. Phys.*, 1996, **104**(17), 6772–6783, DOI: **10.1063/1.471344**.

10 K. Bernardino and A. F. De Moura, Surface Electrostatic Potential and Water Orientation in the Presence of Sodium Octanoate Dilute Monolayers Studied by Means of Molecular Dynamics Simulations, *Langmuir*, 2015, **31**(40), 10995–11004, DOI: **10.1021/acs.langmuir.5b02904**.

11 D. Paik, H. Lee, H. Kim and J. M. Choi, Thermodynamics of π–π Interactions of Benzene and Phenol in Water, *Int. J. Mol. Sci.*, 2022, **23**(17), 9811, DOI: **10.3390/ijms23179811**.

12 H. J. C. Berendsen, J. R. Grigera and T. P. Straatsma, The Missing Term in Effective Pair Potentials, *J. Phys. Chem.*, 1987, **91**(24), 6269–6271, DOI: **10.1021/j100308a038**.

13 U. L. Abbas, Q. Qiao, M. T. Nguyen, J. Shi and Q. Shao, Structure and Hydrogen Bonds of Hydrophobic Deep Eutectic Solvent-Aqueous Liquid–Liquid Interfaces, *AIChE J.*, 2021, **67**(12), 1–12, DOI: **10.1002/aic.17427**.

14 M. Luo, O. A. Mazyar, Q. Zhu, M. W. Vaughn, W. L. Hase and L. L. Dai, Molecular Dynamics Simulation of Nanoparticle Self-Assembly at a Liquid-Liquid Interface, *Langmuir*, 2006, **22**(14), 6385–6390, DOI: **10.1021/la0607196**.

15 M. Luo and L. L. Dai, Molecular Dynamics Simulations of Surfactant and Nanoparticle Self-Assembly at Liquid-Liquid Interfaces, *J. Phys.:Condens. Matter*, 2007, **19**(37), 375109, DOI: **10.1088/0953-8984/19/37/375109**.

16 R. Kurapati and U. Natarajan, New Insights into Adsorption Structure and Hydration of Polymer at Oil-Water Interface Obtained by Molecular Dynamics Simulations: Isotactic Poly(Methacrylic Acid), *Polymer*, 2022, **260**, 125378, DOI: **10.1016/j.polymer.2022.125378**.

17 M. M. Menamparambath, In Situ Engineering of Conducting Polymer Nanocomposites at Liquid/Liquid Interfaces: A

Perspective on Fundamentals to Technological Significance, *ACS Mater. Au*, 2024, **4**(2), 115–128, DOI: **10.1021/acsmaterialsau.3c00068**.

18 X. Hua, J. Frechette and M. A. Bevan, Nanoparticle Adsorption Dynamics at Fluid Interfaces, *Soft Matter*, 2018, **14**(19), 3818–3828, DOI: **10.1039/c8sm00273h**.

19 R. Kurapati and U. Natarajan, Role of Concentration and Hydrophobic Nature of Weak Polyelectrolytes on Adsorption Structure and Thermodynamics at Oil-Water Interface: Study of Several Carboxylate Polymers, *Polymer*, 2023, **285**, 126315, DOI: **10.1016/j.polymer.2023.126315**.

20 E. Guzmán, F. Ortega and R. G. Rubio, Forces Controlling the Assembly of Particles at Fluid Interfaces, *Langmuir*, 2022, **38**(44), 13313–13321, DOI: **10.1021/acs.langmuir.2c02038**.

21 S. K. Chondath, R. R. Poolakkandy, R. Kottayintavida, A. Thekkangil, N. K. Gopalan, S. T. Vasu, S. Athiyanathil and M. M. Menamparambath, Water–chloroform Interface Assisted Microstructure Tuning of Polypyrrole-Silver Sheets, *ACS Appl. Mater. Interfaces*, 2019, **11**(1), 1723–1731, DOI: **10.1021/acsami.8b18943**.

22 Y. Tang, H. T. Wang, M. Chen, D. J. Qian, L. Zhang and M. Liu, Silver(I)-Directed Growth of Metal-Organic Complex Nanocrystals with Bidentate Ligands of Hydroquinine Anthraquinone-1,4-Diyl Diethers as Linkers at the Water–chloroform Interface, *Nanoscale Res. Lett.*, 2014, **9**(1), 1–9, DOI: **10.1186/1556-276X-9-488**.

23 S. K. Chondath, A. P. K. Sreekala, C. Farzeena, S. N. Varanakkottu and M. M. Menamparambath, Interfacial Tension Driven Adsorption of MnO2 Nanoparticles at the Liquid/Liquid Interface to Tailor Ultra-Thin Polypyrrole Sheets, *Nanoscale*, 2022, **14**(31), 11197–11209, DOI: **10.1039/d2nr02130g**.

24 L. Wang, G. Zhu, P. Wang and B.-M. Zhang, Self-Assembling of Polymer-Enzyme Conjugates at Oil Water Interfaces, *Biotechnol. Prog.*, 2005, **21**, 1321–1328, DOI: **10.1021/bp049593y**.

25 M. R. Mahmoudian, W. J. Basirun and Y. Alias, Synthesis of Polypyrrole/Ni-Doped TiO2 Nanocomposites(NCs) as a Protective Pigment in Organic Coating, *Prog. Org. Coat.*, 2011, **71**(1), 56–64, DOI: **10.1016/j.porgcoat.2010.12.010**.

26 M. R. Mahmoudian, W. J. Basirun, Y. Alias and M. Ebadi, Synthesis and Characterization of Polypyrrole/Sn-Doped TiO 2 Nanocomposites(NCs) as a Protective Pigment, *Appl. Surf. Sci.*, 2011, **257**(20), 8317–8325, DOI: **10.1016/j.apsusc.2011.03.075**.

27 R. Rahman Poolakkandy, S. Kaladi Chondath, N. Puthiyottil, D. Davis and M. M. Menamparambath, N-Butanol/Water Interface-Aided Physicochemical Tuning of Two-Dimensional Transition-Metal Oxides, *Langmuir*, 2020, **36**(4), 872–879, DOI: **10.1021/acs.langmuir.9b03362**.

28 M. R. Mahmoudian, Y. Alias, W. J. Basirum and M. Ebadi, Poly(N-Methyl Pyrrole) and Its Copolymer with o-Toluidine Electrodeposited on Steel in Mixture of DBSA and Oxalic Acid Electrolytes, *Curr. Appl. Phys.*, 2011, **11**(3), 368–375, DOI: **10.1016/j.cap.2010.08.006**.

29 K. J. Ahn, Y. Lee, H. Choi, M. S. Kim, K. Im, S. Noh and H. Yoon, Surfactant-Templated Synthesis of Polypyrrole Nanocages as Redox Mediators for Efficient Energy Storage, *Sci. Rep.*, 2015, **5**, 14097, DOI: **10.1038/srep14097**.

30 S. S. Jeon, C. Kim, J. Ko and S. S. Im, Spherical Polypyrrole Nanoparticles as a Highly Efficient Counter Electrode for Dye-Sensitized Solar Cells, *J. Mater. Chem.*, 2011, **21**(22), 8146–8151, DOI: **10.1039/c1jm10112a**.

31 X. Liang, Y. Liu, Z. Wen, L. Huang, X. Wang and H. Zhang, A Nano-Structured and Highly Ordered Polypyrrole-Sulfur Cathode for Lithium-Sulfur Batteries, *J. Power Sources*, 2011, **196**(16), 6951–6955, DOI: **10.1016/j.jpowsour.2010.11.132**.

32 J. Wang, Y. Xu, F. Yan, J. Zhu and J. Wang, Template-Free Prepared Micro/Nanostructured Polypyrrole with Ultrafast Charging/Discharging Rate and Long Cycle Life, *J. Power Sources*, 2011, **196**(4), 2373–2379, DOI: **10.1016/j.jpowsour.2010.10.066**.

33 N. Puthiyottil, A. Palamparambil, S. Kaladi Chondath, S. N. Varanakkottu and M. M. Menamparambath, Interfacial Tension-Impelled Self-Assembly and Morphology Tuning of Poly(3,4-Ethylene Dioxythiophene)/Tellurium Nanocomposites at Various Liquid/Liquid Interfaces, *ACS Appl. Mater. Interfaces*, 2023, **15**(44), 51944–51957, DOI: **10.1021/acsami.3c11726**.

34 J. Pokki, O. Ergeneman, K. M. Sivaraman, B. Özkale, M. A. Zeeshan, T. Lühmann, B. J. Nelson and S. Pané, Electroplated Porous Polypyrrole Nanostructures Patterned by Colloidal Lithography for Drug-Delivery Applications, *Nanoscale*, 2012, **4**(10), 3083–3088, DOI: **10.1039/c2nr30192j**.

35 F. Gao, N. Zhang, X. Fang and M. Ma, Bioinspired Design of Strong, Tough, and Highly Conductive Polyol-Polypyrrole Composites for Flexible Electronics, *ACS Appl. Mater. Interfaces*, 2017, **9**(7), 5692–5698, DOI: **10.1021/acsami.7b00717**.

36 R. M. A. P. Lima, J. J. Alcaraz-Espinoza, F. A. G. Da Silva and H. P. De Oliveira, Multifunctional Wearable Electronic Textiles Using Cotton Fibers with Polypyrrole and Carbon Nanotubes, *ACS Appl. Mater. Interfaces*, 2018, **10**(16), 13783–13795, DOI: **10.1021/acsami.8b04695**.

37 F. Liu, Y. Yuan, L. Li, S. Shang, X. Yu, Q. Zhang, S. Jiang and Y. Wu, Synthesis of Polypyrrole Nanocomposites Decorated with Silver Nanoparticles with Electrocatalysis and Antibacterial Property, *Composites, Part B*, 2015, **69**, 232–236, DOI: **10.1016/j.compositesb.2014.09.030**.

38 X. Yang, L. Li, S. Shang, G. Pan, X. Yu and G. Yan, Facial Synthesis of Polypyrrole/Silver Nanocomposites at the Water/Ionic Liquid Interface and Their Electrochemical Properties, *Mater. Lett.*, 2010, **64**(17), 1918–1920, DOI: **10.1016/j.matlet.2010.05.042**.

39 D. K. Hore, D. S. Walker, L. Mackinnon and G. L. Richmond, Molecular Structure of the Chloroform - Water and Dichloromethane - Water Interfaces, *J. Phys. Chem. C*, 2007, **111**, 8832–8842.

40 D. S. Frost and L. L. Dai, Molecular Dynamics Simulations of Nanoparticle Self-Assembly at Ionic Liquid-Water and Ionic Liquid-Oil Interfaces, *Langmuir*, 2011, **27**(18), 11339–11346, DOI: **10.1021/la202069m**.

41 R. Kurapati and U. Natarajan, Tacticity and Ionization Effects on Adsorption Behavior of Poly(Acrylic Acid) and Poly(Methacrylic Acid) at the CCl4-H2O Interface Revealed by

MD Simulations, *Ind. Eng. Chem. Res.*, 2022, **61**(44), 16500–16516, DOI: **10.1021/acs.iecr.2c02416**.

42 R. Kurapati and U. Natarajan, Effect of Stereo-Chemistry and Hydrophilic Nature of Synthetic Carboxylic Acid Polymers on Conformation, Intermolecular Structure and Hydration at Air-Water Interface, *Comput. Mater. Sci.*, 2023, **230**, 112447, DOI: **10.1016/j.commatsci.2023.112447**.

43 B. Hess, C. Kutzner, D. Van Der Spoel and E. Lindahl, GRGMACS 4: Algorithms for Highly Efficient, Load-Balanced, and Scalable Molecular Simulation, *J. Chem. Theory Comput.*, 2008, **4**(3), 435–447, DOI: **10.1021/ct700301q**.

44 W. Humphrey, A. Dalke and K. Schulten, Sartorius Products, *J. Mol. Graphics*, 1996, **14**, 33–38.

45 W. L. Jorgensen, D. S. Maxwell and J. Tirado-Rives, Development and Testing of the OPLS All-Atom Force Field on Conformational Energetics and Properties of Organic Liquids, *J. Am. Chem. Soc.*, 1996, **118**(45), 11225–11236, DOI: **10.1021/ja9621760**.

46 U. Essmann, L. Perera, M. L. Berkowitz, T. Darden, H. Lee and L. G. Pedersen, A Smooth Particle Mesh Ewald Method, *J. Chem. Phys.*, 1995, **103**(19), 8577–8593, DOI: **10.1063/1.470117**.

47 T. Darden, D. York and L. Pedersen, Particle Mesh Ewald: An N·log(N) Method for Ewald Sums in Large Systems, *J. Chem. Phys.*, 1993, **98**(12), 10089–10092, DOI: **10.1063/1.464397**.

48 H. Attouch and R. Cominetti, A Dynamical Approach to Convex Minimization Coupling Approximation with the Steepest Descent Method, *J. Differ. Equ.*, 1996, **128**(2), 519–540, DOI: **10.1006/jdeq.1996.0104**.

49 G. Bussi, D. Donadio and M. Parrinello, Canonical Sampling through Velocity Rescaling, *J. Chem. Phys.*, 2007, **126**(1), 014101, DOI: **10.1063/1.2408420**.

50 H. J. C. Berendsen, J. P. M. Postma, W. F. Van Gunsteren, A. Dinola and J. R. Haak, Molecular Dynamics with Coupling to an External Bath, *J. Chem. Phys.*, 1984, **81**(8), 3684–3690, DOI: **10.1063/1.448118**.

51 S. Nosé, A Molecular Dynamics Method for Simulations in the Canonical Ensemble, *Molecular Physics: An International Journal at the Interface Between Chemistry and Physics*, 1984, **52**, 255–268.

52 M. Parrinello and A. Rahman, Polymorphic Transitions in Single Crystals: A New Molecular Dynamics Method, *J. Appl. Phys.*, 1981, **52**(12), 7182–7190, DOI: **10.1063/1.328693**.

53 A. K. Mazur, Common Molecular Dynamics Algorithms Revisited: Accuracy and Optimal Time Steps of Störmer-Leapfrog Integrators, *J. Comput. Phys.*, 1997, **136**(2), 354–365, DOI: **10.1006/jcph.1997.5740**.

54 B. Hess, P-LINCS: A Parallel Linear Constraint Solver for Molecular Simulation, *J. Chem. Theory Comput.*, 2008, **4**(1), 116–122, DOI: **10.1021/ct700200b**.

55 H. J. C. Berendsen, J. P. M. Postma, W. F. van Gunsteren and J. Hermans, Interaction Models for Water in Relation to Protein Hydration. In Intermolecular Forces, *Intermol. Forces*, 1981, **3**, 331–342, DOI: **10.1007/978-94-015-7658**.

56 A. Bahramian and A. Danesh, Prediction of Liquid-Liquid Interfacial Tension in Multi-Component Systems, *Fluid Phase Equilib.*, 2004, **221**(1–2), 197–205, DOI: **10.1016/j.fluid.2004.04.012**.

57 P. Taylor, I. G. Tironi and W. F. Gunsteren, A Molecular Dynamics Simulation Study of Chloroform, *Molecular Physics: An International Journal at the Interface Between Chemistry and Physics*, 2006, 37–41, DOI: **10.1080/00268979400101331**.

58 M. Scharf, F. Eisenhaber, P. Lijnzaad and P. Argos, The Double Cubic Lattice Method: Integration of Surface Area and Volume Efficient Approaches to Numerical Molecular Assemblies and to Dot Surface Contouring of Molecular Assemblies, *J. Comput. Chem.*, 1995, **16**(3), 273–284, DOI: **10.1002/jcc.540160303**.

59 Y. Zhang, S. E. Feller, B. R. Brooks and R. W. Pastor, Computer Simulation of Liquid/Liquid Interfaces. I. Theory and Application to Octane/Water, *J. Chem. Phys.*, 1995, **103**(23), 10252–10266, DOI: **10.1063/1.469927**.

60 C. V. Nguyen, C. M. Phan, H. M. Ang, H. Nakahara, O. Shibata and Y. Moroi, Molecular Dynamics Investigation on Adsorption Layer of Alcohols at the Air/Brine Interface, *Langmuir*, 2015, **31**(1), 50–56, DOI: **10.1021/la504471q**.

61 S. M. Kathmann, I. F. W. Kuo and C. J. Mundy, Electronic Effects on the Surface Potential at the Vapor-Liquid Interface of Water, *J. Am. Chem. Soc.*, 2008, **130**(47), 16556–16561, DOI: **10.1021/ja908142d**.

62 D. Van Der Spoel, P. J. Van Maaren, P. Larsson and N. Tîmneanu, Thermodynamics of Hydrogen Bonding in Hydrophilic and Hydrophobic Media, *J. Phys. Chem. B*, 2006, **110**(9), 4393–4398, DOI: **10.1021/jp0572535**.

63 S. Mondal and M. V. Sangaranarayanan, A Novel, Rapid Synthetic Protocol for Controllable Sizes, Conductivities and Monomer Units of Soluble Polypyrrole, *Eur. Polym. J.*, 2015, **71**, 596–611, DOI: **10.1016/j.eurpolymj.2015.08.027**.